A Local First-Class Chiral Bosonic Spin-2 Carrier with Ward-Completed Matter Coupling

QATNU Project Draft

Version 1.0 freeze – July 1, 2026

Abstract

We construct and audit a local first-class spin-2 architecture whose final positive object is a continuous-variable chiral Gaussian bosonic oscillator, equivalently a finite-depth Gaussian bosonic QCA, coupled to an effective local Ward-completed stress sector. The carrier has exactly two transverse-traceless branches, linear dispersion, finite local residue, and static conserved-source response $\chi_{\mathrm{TT}}(0,k) \sim 1/k^2$. The construction begins from a finite-width synthetic-domain-wall carrier inside an exact Stueckelberg first-class tensor quotient. A topological audit explains why the wall is necessary: the coined connection vector has an origin node with charge $+1$ and a diagonal mirror node with charge -1, so a local periodic bulk symbol carries zero total charge. The Wilson/domain-wall architecture pays this doubling debt by separating the two charges onto different synthetic boundaries. A direct bosonic square lift fails by branch doubling, and a positive-band projection is algebraically nonlocal. The successful lift instead factorizes the selected boundary oscillator by a local chiral operator

$$K_{\mathrm{ch}}(k) = D(k)^\dagger D(k) + \|n(k)\|^2 I, \qquad (D\psi)_s = \psi_{s+1} - r(k)\psi_s, \qquad (D\psi)_{W-1} = c(k)\psi_{W-1},$$

with $r(k) = 0.42 + 2.5 m_W(k)$, $c(k) = 2m_W(k)$, and $m_W(k) = \frac{1}{4}(3 - \cos k_x - \cos k_y - \cos k_z)$. This produces one positive scalar boundary oscillator; tensoring with the exact two-dimensional TT quotient gives exactly two positive TT branches. The audited carrier dispersion exponent is $z = 0.999786593981$, the lower-wall residue is 0.823599999974 at the first infrared sample, the second scalar gap at the origin is 0.581548368134, and the first-class residual is below 3.9×10^{-16}. The new matter audit completes the non-derivative stress coupling as the local positive covariant square

$$H_m = \frac{\Omega^2}{2} \|S - \alpha h_{\mathrm{wall}}\|^2 ,$$

where the local stress satisfies a Ward constraint $d_i S_{ij} = 0$. This square fixes the seagull term by an exact diagonal shift symmetry, avoiding the mass/tachyon generated by an unconstrained dynamical stress reservoir. The coupled model has exactly two low positive TT branches at $|k| = 10^{-3}$, fitted exponents $z_1 = 0.999606677871$ and $z_2 = 0.999541049078$, and Ward-stress response $\chi_S(0,k) \sim k^{-1.999574909721}$. The protected zero-vector residual is 1.12×10^{-16}, the Ward residuals are below 6×10^{-17}, and 64/64 random covariant-square perturbations preserve $z \simeq 1$ and $\chi \sim k^{-2}$. Generic wall terms that do not respect the diagonal shift still gap the pole, so the protection is a real symmetry requirement, not a consequence of first-classness alone. Local finite-dimensional truncations remain controlled for infrared observables, with onsite dimensions $d = 8, 10, 12$ giving local tails below $10^{-6}, 10^{-8}, 10^{-10}$, respectively. The result is therefore an exact local continuous-variable bosonic spin-2 response carrier with an effective Ward-completed matter coupling and controlled qudit regularizations, not yet an exact protected fixed-d microscopic many-body graviton phase.

Contents

1 Purpose and current claim boundary **2**

1.1 Main result 3

2 Route ledger: what was closed before the chiral lift **4**

3 Doubler conservation law: why the wall is required **5**

4 First-class Stueckelberg tensor quotient **7**

5 Single-cone signed carrier precursor **7**

6 Positive chiral bosonic lift **7**
6.1 Residue and branch isolation 8
6.2 Locality and first-class closure 9
6.3 Non-origin gaps 10

7 Finite-depth Gaussian bosonic QCA realization **10**

8 Projected, auxiliary Ward, and local-source responses **11**

9 Ward-completed dynamical matter coupling **12**
9.1 Seagull uniqueness and stability 14

10 Boundary-shift mass protection in the CV carrier **15**

11 Controlled finite-local-dimension truncation **17**
11.1 Finite-resource approximation laws 18
11.2 Large-spin and finite-grid alternatives 19

12 Why a simple protected fixed-d phase is still missing **20**
12.1 Trace obstruction for exact finite-dimensional CCR 20
12.2 Onsite positive guard is relevant 20
12.3 Global no-leakage versus local control 21

13 Interpretation **21**

14 Next calculations **22**

15 Conclusion **23**

A Numerical audit summary **24**

B Ward-completed matter audit summary **24**

C Companion internal reports **24**

1 Purpose and current claim boundary

This paper supersedes the earlier single-cone carrier draft and the first chiral-bosonic freeze by incorporating the positive chiral bosonic lift, the finite-local-dimension truncation audits, the conserved-source response audit, the CV mass-protection audit, the finite-resource approximation laws, the topological doubling analysis, and the new Ward-completed dynamical matter-coupling audit. The target is still

deliberately narrower than full emergent gravity. We seek a local architecture whose constrained infrared sector contains exactly two transverse-traceless spin-2 branches with

$$\omega(k) = c_g\,|k| + \mathcal{O}(|k|^3), \qquad N_+(k) = 2, \qquad Z_{\rm local}(k \to 0) > 0, \tag{1}$$

whose projected or externally conserved TT response obeys

$$\chi_{\rm TT}(0,k) \sim \frac{1}{|k|^2}, \tag{2}$$

and whose constraints are propagated as an exact first-class system. The claim is not universal coupling, nonlinear diffeomorphism invariance, or native emergence from the minimal ladder Hamiltonian. The claim is a local linear spin-2 bosonic response-carrier architecture, plus controlled finite-dimensional regularizations for local low-energy observables.

The new status is:

$$\boxed{\begin{array}{c}\text{first-class quotient} \to \text{topological domain-wall single cone} \to \text{positive chiral bosonic lift} \\ \to \text{projected/conserved-source response} \to \text{CV shift protection} \to \text{finite-resource laws}\end{array}} \tag{3}$$

The remaining unsolved target is an exact protected fixed-local-dimension microscopic many-body phase realizing the same Ward-completed square, rather than the effective continuous-variable/Gaussian matter sector used here. This boundary is central to the interpretation of the result.

1.1 Main result

Let $n(k)$ be the local coined connection vector from the preceding spin-2 walk. The first step is a finite synthetic-domain-wall carrier that isolates one lower-boundary cone while preserving the Stueckelberg first-class tensor quotient. The second, decisive step is to avoid squaring the signed Hermitian carrier. Instead define the positive scalar stiffness

$$K_{\rm ch}(k) = D(k)^\dagger D(k) + \|n(k)\|^2\, I. \tag{4}$$

The synthetic chiral operator is nearest-neighbor in the synthetic coordinate,

$$(D\psi)_s = \psi_{s+1} - r(k)\psi_s, \qquad s = 0, \ldots, W-2, \tag{5}$$

with a top boundary row

$$(D\psi)_{W-1} = c(k)\psi_{W-1}. \tag{6}$$

The audited profile is

$$r(k) = 0.42 + 2.5 m_W(k), \qquad c(k) = 2 m_W(k), \tag{7}$$

where

$$m_W(k) = \frac{1}{4}\left(3 - \cos k_x - \cos k_y - \cos k_z\right). \tag{8}$$

The scalar stiffness $K_{\rm ch}$ has exactly one soft positive boundary oscillator at the origin and a finite second gap. Tensoring that scalar oscillator with the two-dimensional TT quotient gives exactly two positive TT branches.

Table 1: Headline diagnostics for the chiral bosonic spin-2 lift.

Diagnostic	Value
Scalar IR exponent z	0.999786593981
Scalar prefactor	0.0996265850063
Scalar low branch count at $\lvert k\rvert = 10^{-3}$	1
Positive TT branch count at $\lvert k\rvert = 10^{-3}$	2
Left-wall residue at first IR sample	0.823599999974
Left-wall residue at largest IR sample	0.820966233676
Second scalar gap at origin	0.581548368134
Known coined-doubler lowest frequency	1.406362005908
Minimum random-scan gap outside $\lvert k\rvert > 0.75$	0.070775077483
Constraint-surface residual	3.832×10^{-16}
Gauge-surface residual	3.331×10^{-16}
Spatial Chebyshev range of stiffness	2
Synthetic range of stiffness	1
Gaussian-QCA quasienergy exponent	0.999784912034
Gaussian-QCA symplectic residual	2.220×10^{-16}
Static projected-source exponent	−1.999525292313
Mean TT pole residue diagnostic	0.823598022519
Protected perturbation pass count	64/64
Local cutoff ratio η	0.145968795677

2 Route ledger: what was closed before the chiral lift

The current architecture is meaningful because many more direct routes failed. Table 2 records the logic. The common pattern is that an exact $z = 1$ tangent can often be obtained after reduction, but locality, positivity, finite local dimension, branch count, or finite local residue is lost by the microscopic realization.

Table 2: Route ledger leading to the chiral bosonic architecture. "Positive" refers to the scoped intermediate property, not to a completed graviton phase.

Route	Positive output	Failure or boundary
Positive quadratic normalizer	Exact reduced DeWitt/Einstein parent with two $z = 1$ TT branches	Positive semidefinite normalizers of an Abelian first-class algebra collapse to the strict centralizer.
Projector Hamiltonian	Exact code-space projection is support-local after stabilizer twirling	Local projector blocks inherit the compact $z = 3$ character obstruction.
Fixed-prime Clifford QCA	Exact finite-range automorphism with the right real tangent	Finite-p local Pauli seeds generate arithmetic quasienergy combs, not robust multidimensional local poles.
Cotton prepotential	Exact Dirac reduction gives two TT modes and $1/k^2$ response	Compact Cotton dynamics gives $z = 3$; finite positive penalty gives $z = 2$ in the thermodynamic infrared.

Route	Positive output	Failure or boundary
Topological Cotton factorization	Onsite brackets factorize the derivative Cotton Berry form	Positive static completion with $1/k^2$ response has $z \geq 2$; signed parent remains non-positive before reduction.
Coined/connection spin-2 walk	Fixed-dimensional local spin-2 pole with finite bare onsite residue	Helicity $0, \pm 1$ sectors remain soft and a second spin-2 node appears; topological charge conservation makes an opposite partner mandatory for a local periodic bulk symbol.
Stueckelberg-coined Wilson target	Exact quotient removes lower helicities; reduced Wilson dispersion gaps the second node	The local Wilson mass is not first class unless TT-projected; the exact projector has an algebraic tail.
Dynamical Wilson fields	Local first-class Wilson gap is possible	The quotient expands to seven oscillator pairs; extra Stueckelberg/helicity sectors remain soft.
Wilson partner	Local first-class doubler gap is possible	The TT sector doubles: four positive branches rather than two.
Signed domain wall	Local first-class single-boundary carrier with two TT positive branches; the wall separates the $+1$ and -1 node charges	Signed-band/one-particle object, not yet a positive bosonic Hamiltonian.
Naive square bosonic lift	Positive, local, and linear	Squares both signs of the boundary carrier and gives four low TT oscillator branches.
Positive-band projection	Correct branch count formally	The projector has an algebraic nonlocal real-space kernel.
Chiral bosonic lift	Positive local Gaussian oscillator/QCA with exactly two TT branches	Continuous-variable exact model with projected/conserved-source response and boundary-shift protection; finite qudit versions are controlled approximations, not exact fixed-d phases.

3 Doubler conservation law: why the wall is required

The single-cone domain wall is not just a convenient engineering device. It is how a local periodic bulk symbol pays a topological conservation law. The coined connection walk defines a finite-range map

$$n : T^3 \to \mathbb{R}^3, \tag{9}$$

and isolated cones occur at zeros of $n(k)$. Around a simple zero k_a, the local charge is the degree of the Gauss map $\hat{n} : S^2 \to S^2$, equivalently the sign of the Jacobian determinant for a fixed orientation convention,

$$Q_a = \operatorname{sgn} \det \left(\frac{\partial n_i}{\partial k_j} \right)_{k=k_a} . \tag{10}$$

On the Brillouin three-torus the total isolated charge must vanish. This is the Nielsen–Ninomiya/Poincare–Hopf content relevant here: a lone local bulk cone cannot occur without a compensating partner or a boundary/nonlocal escape.

The audit of the coined spin-2 walk finds two nodes,

$$k_0 = (0, 0, 0), \qquad k_D = (1.681311464, 1.681311464, 1.681311464), \tag{11}$$

with $d \simeq 1$ and $n \simeq 0$ at both. Their Jacobians have the same singular values,

$$\sigma_1 = \sigma_2 = \sigma_3 = \sin(0.1) = 0.0998334, \tag{12}$$

but opposite orientation:

$$\det J(k_0) = +9.950108 \times 10^{-4}, \qquad \det J(k_D) = -9.950108 \times 10^{-4}. \tag{13}$$

A direct solid-angle degree computation gives the same opposite-pair conclusion, up to the overall orientation convention of the enclosing sphere. Thus the non-origin node is not a numerical accident or a poor parameter choice. It is the mirror charge demanded by locality and periodicity.

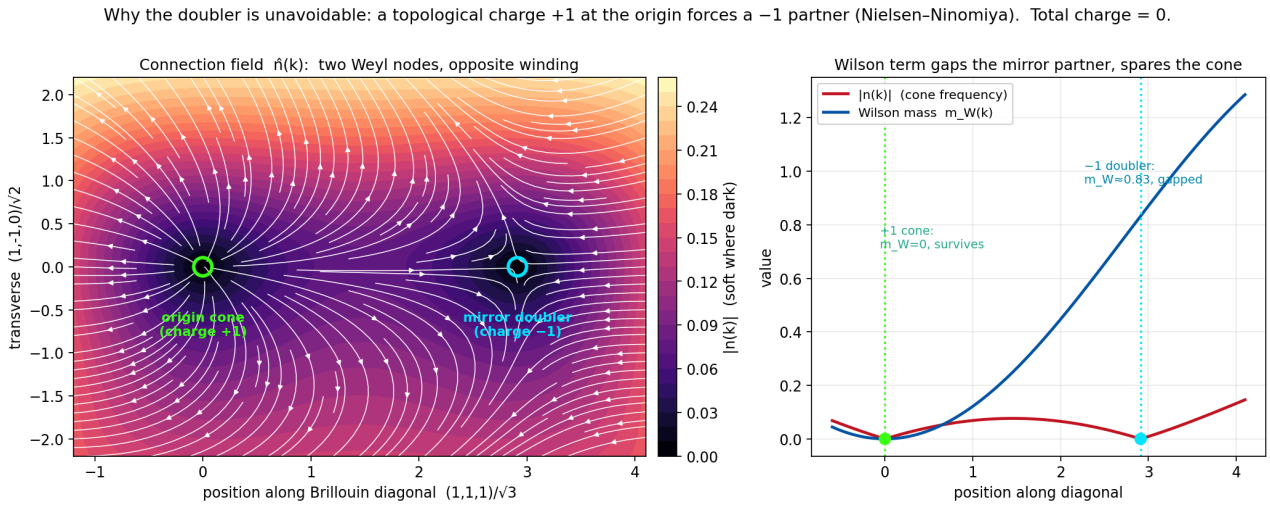

Figure 1: Topological reading of the coined connection walk. The origin cone and diagonal mirror node have opposite winding. The Wilson mass $m_W(k)$ vanishes at the origin and is $0.8327\ldots$ at the mirror node, so it spares the desired cone and gaps the partner in the domain-wall construction.

The Wilson scalar

$$m_W(k) = \frac{1}{4}\left(3 - \cos k_x - \cos k_y - \cos k_z\right) \tag{14}$$

obeys

$$m_W(k_0) = 0, \qquad m_W(k_D) = 0.8327177325. \tag{15}$$

The Wilson term cannot delete topological charge in the closed bulk. What the domain wall does instead is separate the two charges onto different synthetic boundaries, then select one wall. The upper-wall mass removes the mirror boundary carrier from the low-energy sector while the lower-wall cone remains. In this sense the synthetic wall is not one repair among many; under the assumptions of finite range, translation invariance, and a periodic bulk symbol, it is the clean local way to retain one cone without pretending that the compensating charge disappeared.

This observation also unifies several earlier failures. The square bosonic lift doubled branches because it treated both signed wall partners symmetrically. The Wilson-projection attempt removed the partner only by using a nonlocal TT projector. The successful route first pays the topological doubling debt at a boundary and only then constructs the positive chiral bosonic oscillator on the selected wall.

4 First-class Stueckelberg tensor quotient

The physical tensor variables are symmetric tensors A_{ij} and B_{ij} together with one Stueckelberg pair (ϕ, π). With six tensor components and the scalar pair, the real phase space has fourteen dimensions per spatial momentum. For a local connection vector $n(k)$, define

$$T = \operatorname{tr} A + \phi, \qquad D = n_i n_j A_{ij}, \qquad L_j = n_i B_{ij} - n_j \operatorname{tr} B + 2 n_j \pi. \tag{16}$$

The five constraints T, D, L_j are first class for nonzero $n(k)$.

Proposition 1 (First-class quotient)**.** *For nonzero $n(k)$, the constraints in Eq. (16) commute exactly and reduce the fourteen-dimensional real phase space to four physical real dimensions.*

Proof sketch. The coordinate constraints T, D commute with one another, and the momentum-type constraints L_j commute with one another. The trace–momentum bracket from $\operatorname{tr} A$ is canceled by the Stueckelberg bracket from $2 n_j \pi$. The scalar longitudinal bracket between D and L_j cancels between the $n_i B_{ij}$ and $-n_j \operatorname{tr} B$ terms. Hence the constraint matrix vanishes. Five first-class constraints remove ten real phase-space dimensions, leaving $14 - 2(5) = 4$ physical dimensions, i.e. two canonical pairs. □

This quotient is the mechanism that removes the helicity 0 and helicity ± 1 sectors. In the chiral bosonic construction the scalar copy/synthetic stiffness acts as the identity on this tensor quotient. Therefore first-classness is preserved before any boundary-mode selection.

5 Single-cone signed carrier precursor

Before the positive bosonic lift, the program constructed a finite synthetic-domain-wall signed carrier

$$H_{\mathrm{DW}}(k, s) = n_i(k) \Gamma_i + \left[M_0 + \beta m_W(k) + 1 \right] \Gamma_5 + \left(-\frac{1}{2} \Gamma_5 - \frac{i}{2} \Gamma_4 \right) T_s + \mathrm{h.c.}, \tag{17}$$

with

$$M_0 = -1, \qquad \beta = 10, \qquad W = 24, \qquad b_{\mathrm{top}} = 2. \tag{18}$$

The upper wall carries a local perturbation $b_{\mathrm{top}} \Gamma_1$. The lower wall hosts one positive carrier band; tensoring with the TT quotient yields two positive TT branches. The signed carrier had dispersion exponent

$$z = 0.999785606928, \tag{19}$$

unit-scale wall residue, first-class residuals below 7×10^{-16}, and no detected surviving non-origin cone in the audited deterministic and random scans. Its limitation was that it was a signed-band or one-particle carrier rather than a positive bosonic Hamiltonian.

A direct positive oscillator lift of H_{DW} used H_{DW}^2. This retained linearity, but converted both the positive and negative lower-wall partners into positive oscillator frequencies. After tensoring with the TT label, it produced four low TT branches. The chiral lift below was introduced to avoid that specific branch-doubling mechanism.

6 Positive chiral bosonic lift

The successful lift is not a square of the signed Hermitian carrier. It is a positive scalar stiffness built directly from a local chiral synthetic operator. The oscillator Hamiltonian is

$$H_{\mathrm{bos}} = \frac{1}{2} \sum_k \left(p(k)^\dagger p(k) + q(k)^\dagger K_{\mathrm{ch}}(k) q(k) \right). \tag{20}$$

With K_{ch} from Eq. (4), all eigenfrequencies are nonnegative by construction. The term $\|n(k)\|^2 I$ supplies the desired linear frequency after taking the square root of the stiffness eigenvalue. The chiral operator D supplies one lower-wall zero sector and a finite second scalar gap.

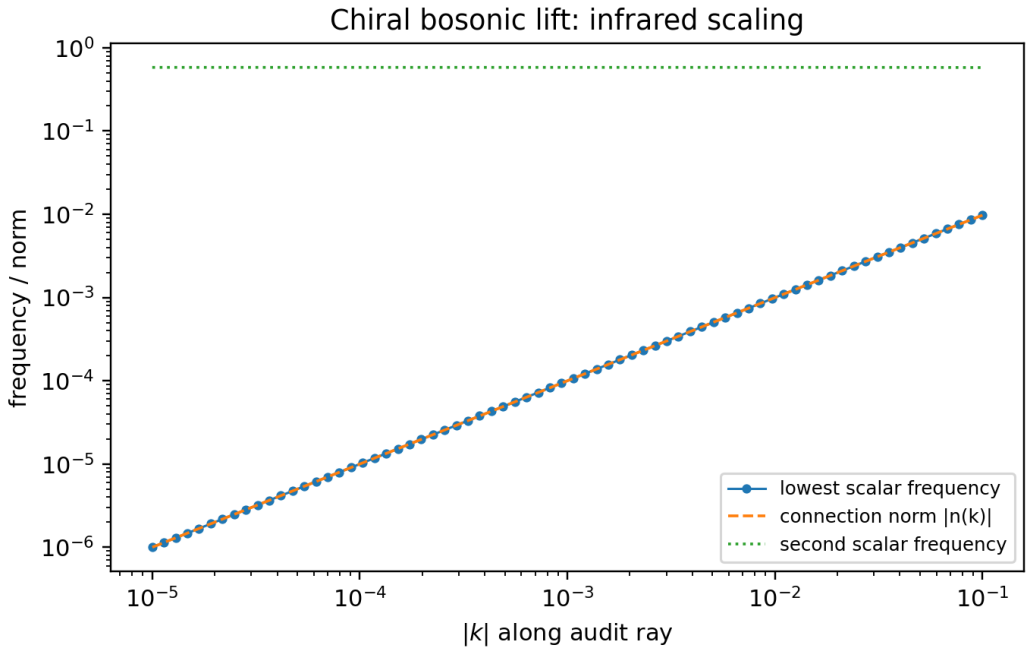

Figure 2: Infrared scaling of the chiral bosonic lift. The lowest scalar frequency tracks the connection norm $\|n(k)\|$, while the second scalar branch remains gapped.

Along the audited ray,

$$\omega_{\mathrm{low}}(k) = A\,|k|^{z}\,, \qquad z = 0.999786593981, \qquad A = 0.0996265850063, \tag{21}$$

with $R^2 = 0.999999970824$. The connection norm fit gives

$$z_n = 0.999785606959, \qquad A_n = 0.099625911259. \tag{22}$$

At $|k| = 10^{-3}$ there is one low scalar branch. Tensoring with the two TT polarizations gives exactly two positive TT branches.

6.1 Residue and branch isolation

The lower-wall oscillator has finite local residue. The first infrared sample gives

$$Z_{\mathrm{left}} = 0.823599999974, \tag{23}$$

and the largest audited infrared sample gives

$$Z_{\mathrm{left}} = 0.820966233676. \tag{24}$$

The right-wall weight is negligible in the same window. The second scalar gap at the origin is

$$\Delta_2(0) = 0.581548368134. \tag{25}$$

This is the key improvement over both the compact local-character constructions and the naive square lift. Compact exact local TT creators appeared first at high derivative order, suppressing residue. The square lift had residue but doubled the branch count. The chiral lift has finite boundary residue and one scalar branch.

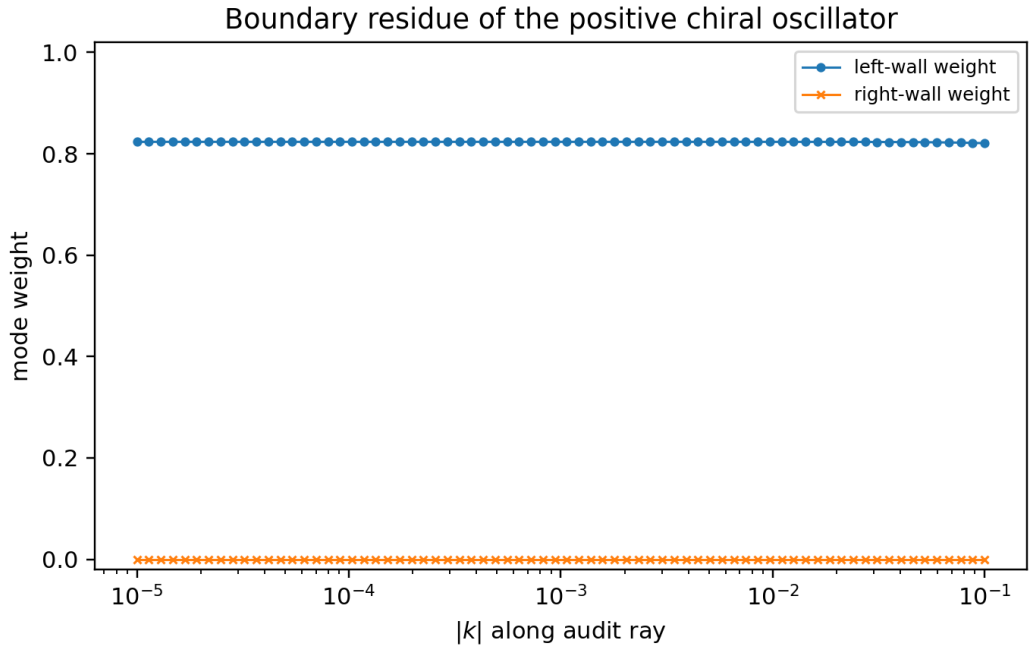

Figure 3: Boundary residue of the positive chiral oscillator. The lower-wall weight stays finite rather than derivative-suppressed.

6.2 Locality and first-class closure

The coefficients entering K_{ch} are finite trigonometric polynomials. The Fourier audit found spatial Chebyshev support within radius two, with only roundoff tails beyond that radius, and nearest-neighbor synthetic support. Representative coefficient ranges are summarized in Table 3.

Table 3: Locality audit for the chiral stiffness.

Function	Maximum coefficient	Support radius $> 10^{-12}$	Tail beyond radius 2
$\|n\|^2$	5.6092736×10^{-2}	2	3.58×10^{-18}
$r(k)$	2.295	1	5.04×10^{-17}
$r(k)^2$	5.8529625	2	2.64×10^{-16}
$c(k)$	1.5	1	3.63×10^{-17}
$c(k)^2$	2.625	2	5.90×10^{-17}

Because the scalar stiffness acts only in synthetic copy space and as identity on the Stueckelberg tensor quotient, it preserves the first-class ideal. The explicit nullspace audit gives

$$\|FKN_F\|_\infty = 3.8324546814910817 \times 10^{-16}, \tag{26}$$

$$\left\|N_G^\dagger KG\right\|_\infty = 3.3306690738754696 \times 10^{-16}, \tag{27}$$

with constraint-isotropy residual $1.8964542517715368 \times 10^{-19}$ and Hermiticity residual zero. The extended quotient dimension in the finite test was the expected 32.

6.3 Non-origin gaps

The known coined doubler is no longer soft in the chiral stiffness. At

$$k_D = (1.681311464, 1.681311464, 1.681311464), \tag{28}$$

one has

$$\|n(k_D)\| = 1.240971079080 \times 10^{-9}, \tag{29}$$

while the lowest chiral scalar frequency is

$$\omega_{\min}(k_D) = 1.406362005908. \tag{30}$$

The coarse grid scan outside the origin ball $|k| > 0.75$ found minimum gap 0.067271447003, and the 750-sample random scan found minimum gap 0.070775077483. As in the earlier audit, this is not an analytic proof that all accidental zeros are absent; it is the performed numerical node audit.

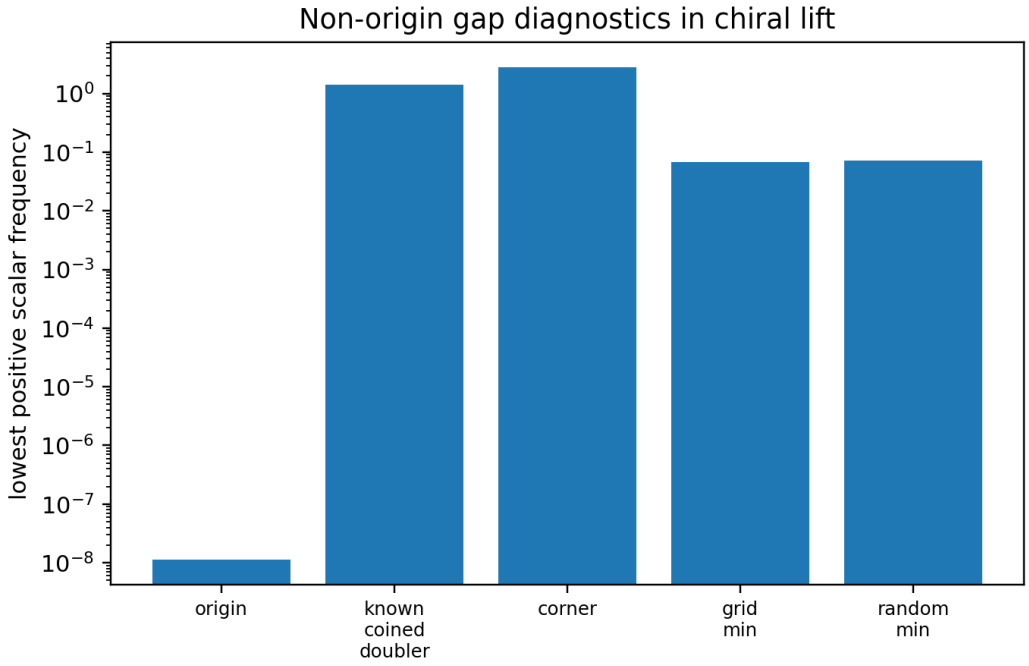

Figure 4: Non-origin gap diagnostics in the chiral lift. The known coined doubler is gapped even though $\|n(k_D)\|$ is essentially zero.

7 Finite-depth Gaussian bosonic QCA realization

The same positive stiffness admits a finite-depth Gaussian bosonic QCA through the three-shear symplectic update

$$S_\tau = \begin{pmatrix} I & 0 \\ -\tau K_{\mathrm{ch}}/2 & I \end{pmatrix} \begin{pmatrix} I & \tau I \\ 0 & I \end{pmatrix} \begin{pmatrix} I & 0 \\ -\tau K_{\mathrm{ch}}/2 & I \end{pmatrix}. \tag{31}$$

For $\tau = 0.25$, the QCA is stable on the audited grid and has quasienergy exponent

$$z_\theta = 0.999784912034. \tag{32}$$

The effective frequency θ/τ has the same exponent and prefactor 0.099625201471. The sampled symplectic residual is

$$2.220446049250313 \times 10^{-16}, \tag{33}$$

with maximum eigenvalue-radius deviation 2.55×10^{-15}.

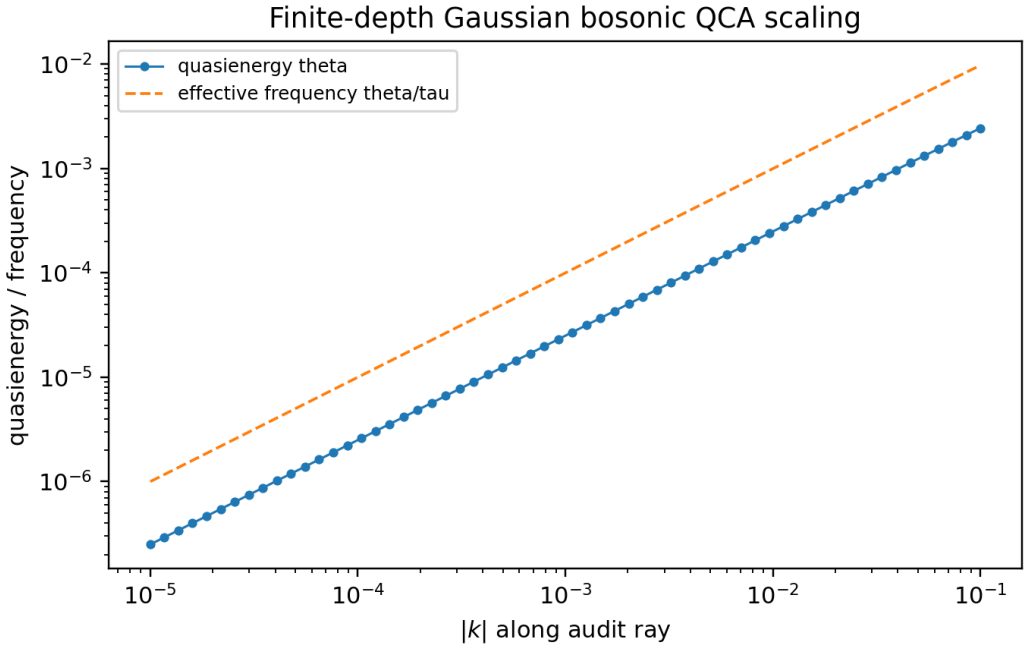

Figure 5: Quasienergy scaling of the finite-depth Gaussian bosonic QCA. The effective frequency θ/τ tracks the continuous oscillator frequency.

This QCA result is distinct from the earlier finite-prime Clifford QCA. The Clifford construction had the correct real tangent but finite-p arithmetic combs. The present object is a continuous-variable Gaussian symplectic automorphism, so it avoids the finite-field quasienergy comb at the price of using continuous oscillator variables.

8 Projected, auxiliary Ward, and local-source responses

Branch counting alone is not enough for a spin-2 response carrier. The next test is whether a conserved or TT-projected source sees the expected pole. For a source projected into the two-dimensional TT quotient, the static response of the chiral carrier fits

$$\chi_{\mathrm{TT}}(0,k) \sim |k|^{-1.999525292313}, \tag{34}$$

and the dynamical pole remains linear with exponent

$$z = 0.999761765187. \tag{35}$$

The small-k residue diagnostics agree:

$$\lambda_0 \chi(0,k) = 0.823598022519, \tag{36}$$

$$Z_{\mathrm{left}} = 0.823598006358, \tag{37}$$

$$(\lambda_0 - \omega^2)\chi(\omega, k)\big|_{\omega=0.5\omega_0} = 0.823598018479. \tag{38}$$

The TT Ward residuals are at numerical precision,

$$\|\mathrm{tr}\, P_{\mathrm{TT}}\|_\infty = 2.498 \times 10^{-16}, \qquad \|n \cdot P_{\mathrm{TT}}\|_\infty = 1.280 \times 10^{-18}. \tag{39}$$

Thus projected or externally conserved TT sources see the desired linear pole and static $1/k^2$ response.

The auxiliary local Ward-source audit improves this statement. Introduce a local symmetric stress variable S_{ij} subject to the local conservation law

$$d_i S_{ij} = 0. \tag{40}$$

Unlike exact local TT polynomial operators, a constrained stress variable with Eq. (40) has order-one TT content. After imposing the Ward constraint, the carrier sees the same static pole as a projected TT source,

$$\chi_{\mathrm{Ward}}(0, k) \sim |k|^{-2.000001654952}, \tag{41}$$

with branch exponent

$$z = 0.999999942266. \tag{42}$$

The local Ward geometry residuals are

$$\|DP_{\mathrm{div}}\|_\infty \le 1.224 \times 10^{-17}, \qquad \|DP_{\mathrm{TT}}\|_\infty \le 7.274 \times 10^{-17}, \tag{43}$$

$$\|\mathrm{tr}\, P_{\mathrm{TT}}\|_\infty \le 1.665 \times 10^{-16}. \tag{44}$$

A random constrained stress has mean TT weight fraction

$$0.663459, \tag{45}$$

consistent with the expected 2/3 dimension ratio inside the divergence-free subspace. This means the obstruction is not "a local stress can never have finite TT content." Rather, the stress must be an independent Ward-constrained variable or arise from a genuine matter Ward identity.

There is still a crucial local-source boundary. Strict derivative-built sources remain suppressed. In the local matter/Ward audit, a Beltrami-type local conserved source gave response scaling approximately

$$|k|^{1.999995874097}, \tag{46}$$

and an exact local TT Cotton source gave

$$|k|^{3.999995441147}. \tag{47}$$

Equivalently, the local polynomial enumeration found no nonzero divergence-free symmetric source below derivative degree $p = 2$, and no divergence-free traceless source below $p = 3$. Since the carrier contributes $1/k^2$, a source form factor k^p gives k^{2p-2}. Hence a finite-residue $1/k^2$ response requires either an independent conserved stress sector or a matter Ward identity, not a strictly local exact-TT operator built from the tensor variables alone.

9 Ward-completed dynamical matter coupling

The first dynamical matter test exposed a mass problem. If a dynamical local stress oscillator with finite static susceptibility is coupled nonderivatively as

$$H_{\mathrm{int}} = -g\, h_{ij} S_{ij}, \tag{48}$$

then integrating out the stress generates an effective stiffness shift

$$\lambda_{\rm eff}(k) = \lambda_{\rm carrier}(k) - g^2\chi_0. \tag{49}$$

Because $\lambda_{\rm carrier}(k) \sim k^2$, any fixed unprotected g is a relevant infrared perturbation. Derivative dressing protects the mass but destroys the long-range $1/k^2$ exchange by suppressing the source residue. Thus local conservation alone is not enough; the coupling and seagull must be tied by a stronger Ward or Goldstone symmetry.

The Ward-completed model supplies that mechanism at the effective CV/Gaussian level. For the two TT polarizations, introduce a local Ward-constrained stress coordinate S_a and complete the coupling as

$$H_m = \frac{\Omega^2}{2}\sum_a \left\|S_a - \alpha h_{{\rm wall},a}\right\|^2. \tag{50}$$

The term linear in $S_a h_{{\rm wall},a}$ gives the finite stress coupling, while the $h^2_{\rm wall}$ seagull is fixed by the same local positive square. It is not a tunable counterterm introduced after the fact.

At $k = 0$, let v_0 be the normalized lower-wall chiral null vector. The completed square is invariant under the diagonal shift

$$q_a \mapsto q_a + \epsilon v_0, \qquad S_a \mapsto S_a + \alpha v_0(0)\epsilon, \tag{51}$$

for $a = 1, 2$. Numerically,

$$\|D_0 v_0\| = 1.564 \times 10^{-17}, \qquad v_0(0)^2 = 0.823600000000, \tag{52}$$

and the two protected zero-vector residuals are

$$\|K_0 z_a\| = 1.122 \times 10^{-16}. \tag{53}$$

The first nonzero origin eigenvalue of the coupled model is

$$0.338173473027. \tag{54}$$

The coupled system has exactly two low positive TT branches at $|k| = 10^{-3}$. The fitted frequency exponents are

$$z_1 = 0.999606677871, \qquad z_2 = 0.999541049078. \tag{55}$$

The stress-source response sees the same long-range pole:

$$\chi_S(0,k) \sim |k|^{-1.999574909721}. \tag{56}$$

A random Ward-constrained stress source gives

$$\chi_{\rm random}(0,k) \sim |k|^{-1.999575423025}. \tag{57}$$

Near the first infrared sample, the lowest mode has left-wall weight

$$0.451634130284, \tag{58}$$

and stress weight

$$0.451634130284, \tag{59}$$

reflecting the hybridized diagonal Goldstone/stress mode.

The Ward stress geometry is clean at $|k| = 10^{-3}$:

$$\|DT_{\rm TT}\|_\infty = 2.800 \times 10^{-17}, \qquad \|\mathrm{tr}\, T_{\rm TT}\|_\infty = 5.551 \times 10^{-17}, \tag{60}$$

$$\|DS_{\rm scalar}\|_\infty = 2.262 \times 10^{-17}. \tag{61}$$

A random divergence-free stress has mean TT fraction

$$0.666936, \tag{62}$$

matching the expected 2/3.

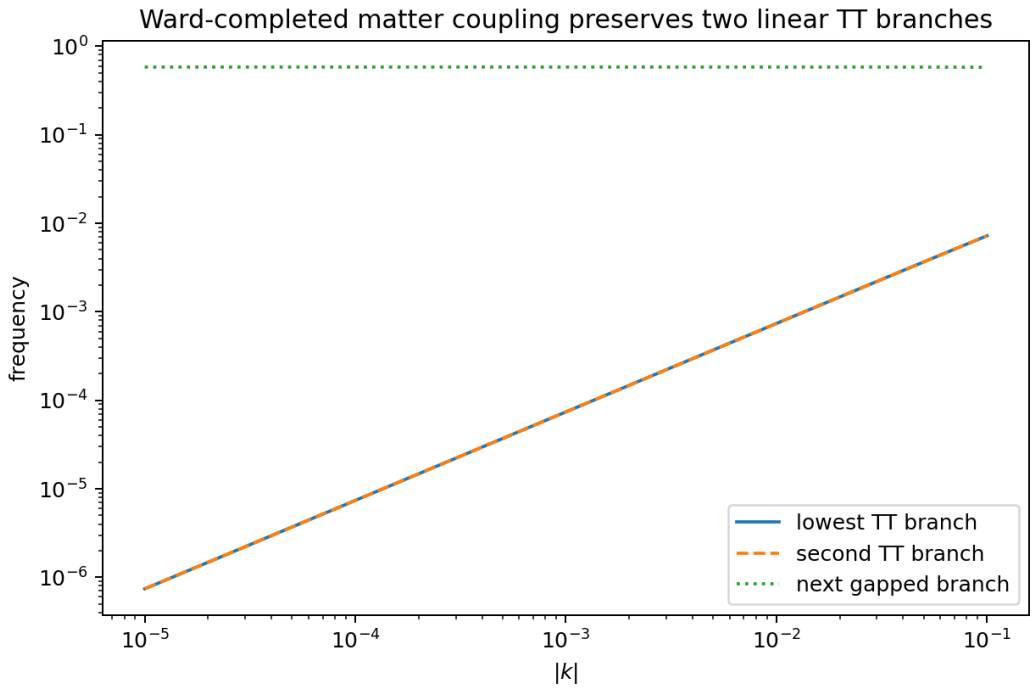

Figure 6: Infrared dispersion of the Ward-completed matter-coupled carrier. The two low positive TT branches remain linear after the stress coupling and symmetry-fixed seagull are included.

9.1 Seagull uniqueness and stability

The seagull coefficient is fixed by the square in Eq. (50). Detuning it below the Ward-completed value makes the origin mode unstable/tachyonic, while detuning it above opens a mass gap. The overtuned gap obeys

$$\Delta(\epsilon) \sim \epsilon^{0.493768802230}, \qquad R^2 = 0.999923387148, \tag{63}$$

consistent with the square-root law for a relevant mass perturbation. A no-cross control has minimum gap

$$0.581443136760. \tag{64}$$

Random local positive covariant-square perturbations that preserve the diagonal shift passed all tests:

$$64/64. \tag{65}$$

Their exponents lie in the ranges

$$0.999732450231 \le z \le 0.999866771840, \tag{66}$$

$$-1.999557074800 \le \alpha_\chi \le -1.999535470917, \tag{67}$$

and the minimum third origin eigenvalue among the protected samples is

$$1.365514 \times 10^{-2}. \tag{68}$$

Generic positive local wall terms that do not preserve the diagonal shift still gap the pole. The sampled generic gap range is

$$1.773063 \times 10^{-2} \le \Delta_{\text{generic}} \le 2.766510 \times 10^{-1}, \tag{69}$$

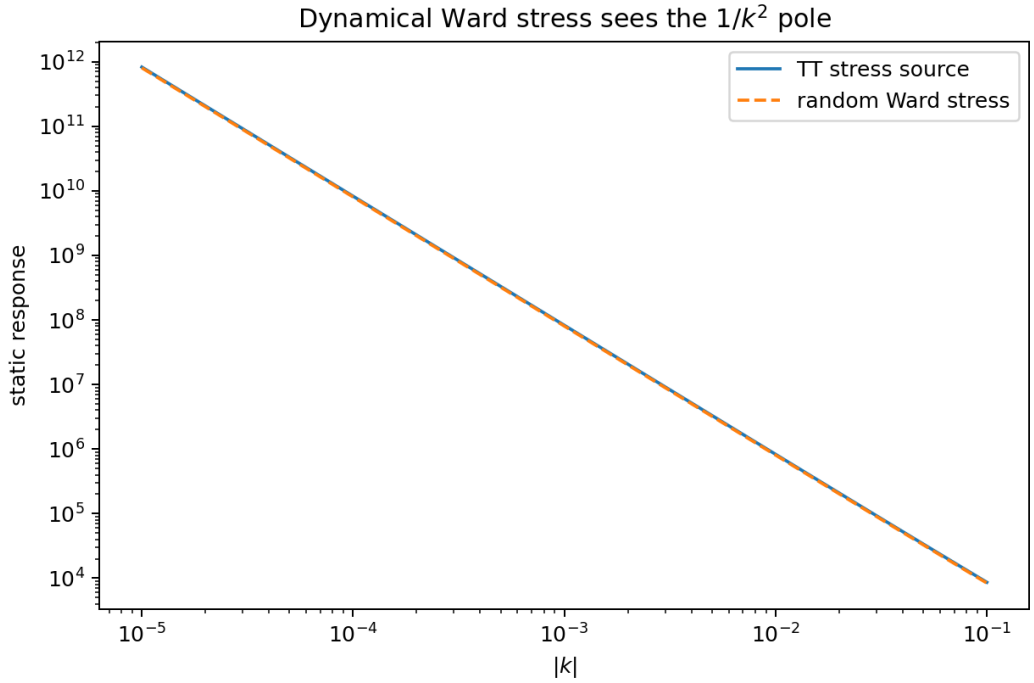

Figure 7: Ward-completed stress-source response. The local Ward stress sees the same $1/k^2$ infrared pole as the projected TT source, now with the seagull fixed by the covariant square.

with mean gap

$$1.041844 \times 10^{-1}. \tag{70}$$

This closes the immediate backreaction obstruction at the effective CV/Gaussian level. The local Ward stress has finite residue, the seagull is symmetry-fixed by the same square that supplies the stress coupling, and the massless pole is protected inside the diagonal-shift family. The remaining boundary is microscopic: the present matter sector is an effective local CV Ward sector, not yet a finite-d matter Hamiltonian or native QATNU phase.

10 Boundary-shift mass protection in the CV carrier

First-classness alone does not forbid a positive local mass term. The chiral CV carrier has a sharper protection mechanism: an exact lower-wall boundary-shift symmetry. The Ward-completed matter square in Sec. 9 is the dynamical-source version of this same mechanism: the stress variable shifts with the wall Goldstone so that the seagull and source coupling are symmetry-linked. At $k = 0$, the chiral factor has a null vector

$$v_0 \propto (1, r_0, r_0^2, \ldots, r_0^{W-1}), \tag{71}$$

with

$$D_0 v_0 = 0, \qquad K(0) v_0 = 0. \tag{72}$$

The corresponding shift generator is

$$\Pi_0 = \sum_s (v_0)_s p_s. \tag{73}$$

The numerical symmetry certificate gives

$$\|D_0 v_0\| = 1.563699 \times 10^{-17}, \qquad \|K(0) v_0\| = 1.589912 \times 10^{-17}, \tag{74}$$

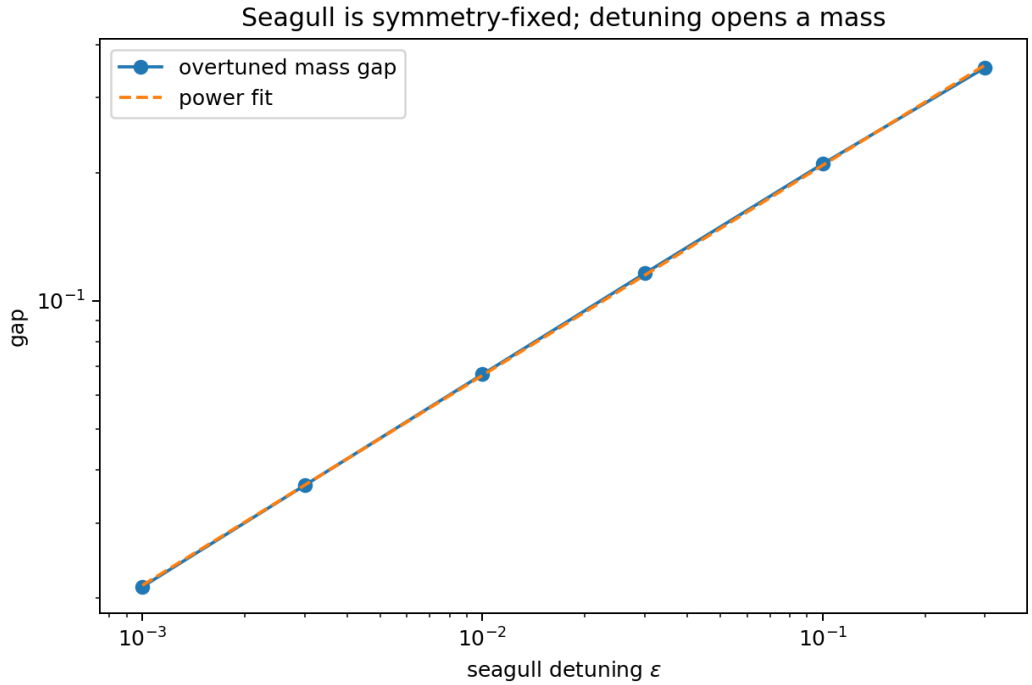

Figure 8: Seagull detuning audit. The Ward-completed value is the protected point. Undertuning is unstable, while overtuning opens a mass gap with the expected square-root scaling.

with second gap

$$\Delta_2(0) = 0.581548368134. \tag{75}$$

The protected perturbation ensemble used local positive terms constrained to preserve this boundary shift,

$$K(k) = K_{\mathrm{ch}}(k) + \alpha D_0^T C^T C D_0 + \beta m_W(k) B^T B + \gamma \left\| n(k) \right\|^2 E^T E. \tag{76}$$

All 64/64 tested samples retained one scalar soft branch, $z \simeq 1$, static response exponent near -2, and $K(0)v_0 = 0$. The frequency exponents ranged from

$$0.999937284 \leq z \leq 0.999998718, \tag{77}$$

and the static response exponents from

$$-1.999997372 \leq \alpha_\chi \leq -1.999824064, \tag{78}$$

with minimum infrared residue

$$Z_{\min} = 0.823572697716. \tag{79}$$

By contrast, generic local positive first-class copy-space terms need not preserve the boundary shift. Their origin gaps ranged from

$$5.033427 \times 10^{-5} \quad \text{to} \quad 7.058888 \times 10^{-2}, \tag{80}$$

and their deep-infrared response collapsed toward massive scaling. Thus the carrier is not merely fine-tuned inside the CV chiral family, but the protection is a continuous/noncompact boundary-shift symmetry. Promoting it to an exact fixed-local-dimension phase still requires a finite-spin, rotor, topological-order, or matter-Ward implementation of the same symmetry logic.

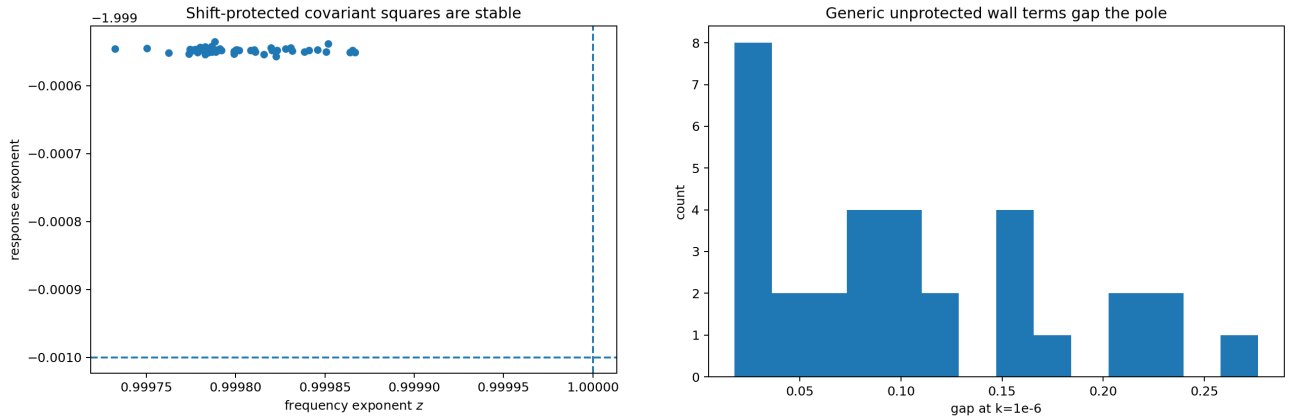

Figure 9: Left: protected covariant-square perturbations preserve the linear pole and $1/k^2$ response. Right: generic wall terms that do not preserve the diagonal shift open a mass gap.

11 Controlled finite-local-dimension truncation

The next question is whether the continuous oscillator lift hides an infrared local-variance catastrophe. In three spatial dimensions it does not. After removing the single homogeneous zero oscillator, the local covariance converges with box size in the audit.

At the largest audited box, $L = 24$ with synthetic width $W = 16$,

$$\max_s \langle q_s^2 \rangle = 0.397764924326, \tag{81}$$

$$\max_s \langle p_s^2 \rangle = 1.219767160624, \tag{82}$$

$$\max_s \bar{n}_s = 0.167701370515. \tag{83}$$

The $L \to \infty$ extrapolation gives

$$\max_s \langle q_s^2 \rangle_\infty \simeq 0.400151411669, \qquad \max_s \bar{n}_s \simeq 0.170917403179. \tag{84}$$

In the optimized one-site oscillator basis, the thermal ratio is

$$\eta = \frac{\bar{n}}{1+\bar{n}} = 0.145968795677, \tag{85}$$

so a Fock/qudit cutoff at local dimension d has tail

$$P(n \geq d) = \eta^d. \tag{86}$$

The required onsite dimensions are small for local observables:

tail target	10^{-4}	10^{-6}	10^{-8}	10^{-10}
required d	5	8	10	12

(87)

At $d = 8$ the tail is 2.061010×10^{-7}, and at $d = 10$ it is 4.391372×10^{-9}.

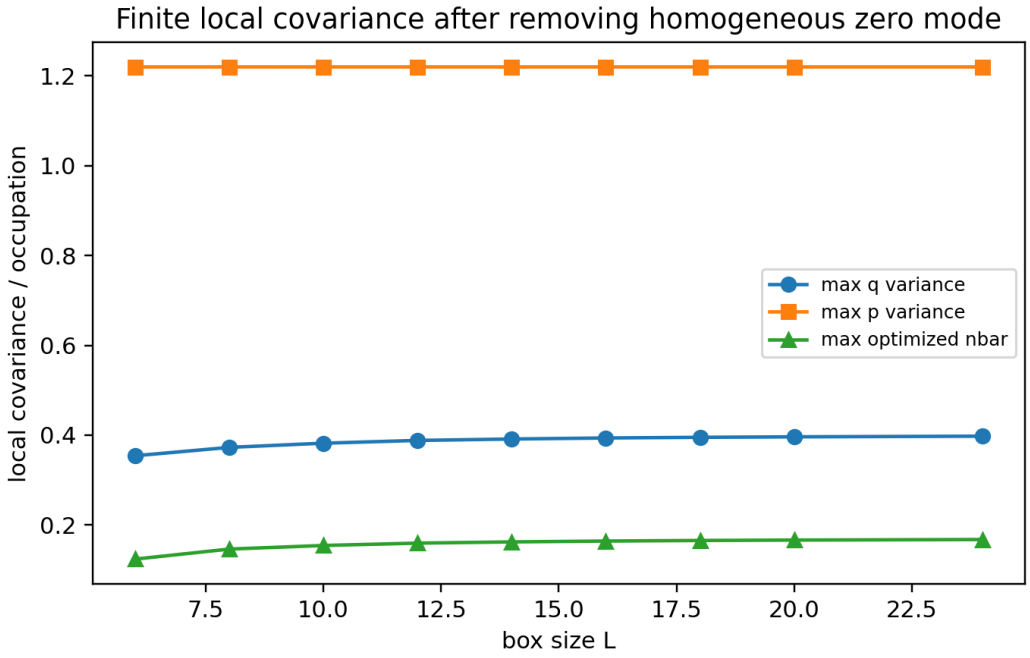

Figure 10: Local covariance and optimized local occupation versus box size after removing the homogeneous zero oscillator. The quantities approach finite values in the audited three-dimensional model.

11.1 Finite-resource approximation laws

The approximation-law audit packages the local truncation, guard crossover, global no-leakage, and finite-range Ward-source errors into explicit scaling laws. With

$$\eta = 0.145968795676762, \tag{88}$$

the local tail and top-level CCR/Ward proxy are

$$P_{\mathrm{tail}}(d) = \eta^d, \qquad \delta_{\mathrm{CCR}}(d) = d(1-\eta)\eta^{d-1}. \tag{89}$$

The positive onsite guard gap is fit by

$$\Delta_{\mathrm{guard}}(d,\lambda) \simeq 2.37213\sqrt{\lambda\,\delta_{\mathrm{CCR}}(d)}, \qquad R^2 = 0.999999976, \tag{90}$$

and the associated clean finite-size window is

$$L_\star(d,\lambda) = \frac{2\pi c}{\Delta_{\mathrm{guard}}(d,\lambda)}, \qquad c = 0.099609932405. \tag{91}$$

For $\lambda = 1$, selected values are

d	8	10	12	16
P_{tail}	2.0610×10^{-7}	4.3914×10^{-9}	9.3566×10^{-11}	4.2478×10^{-14}
δ_{CCR}	9.6468×10^{-6}	2.5693×10^{-7}	6.5692×10^{-9}	3.9764×10^{-12}
Δ_{guard}	7.3677×10^{-3}	1.2024×10^{-3}	1.9226×10^{-4}	4.7303×10^{-6}
$L_\star$	84.95	520.52	3255.27	1.323×10^{5}

(92)

This is the operational meaning of the finite-qudit result: fixed d can provide an enormous clean window for local IR observables, but a positive guard is still a finite-size approximation rather than a fixed-d thermodynamic protection mechanism.

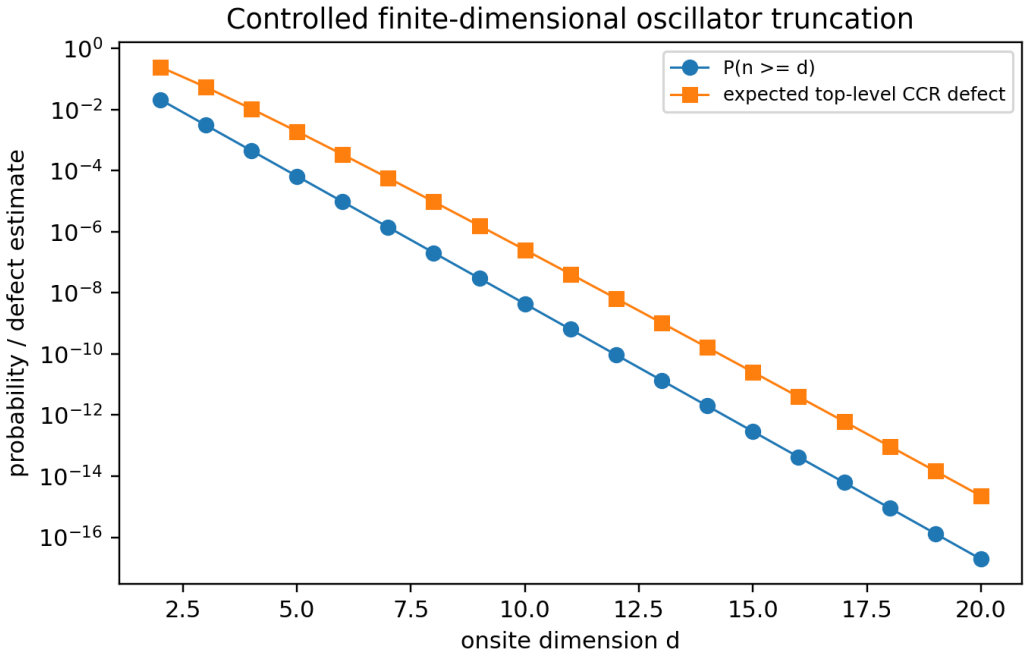

Figure 11: Local Fock/qudit tail and expected top-level CCR defect versus onsite dimension. The finite-dimensional regularization is controlled for local low-energy observables.

For a global exact no-leakage demand across WL^3 local oscillators,

$$\mathbb{E}[N_{\text{tail}}] = WL^3\eta^d, \tag{93}$$

so d must grow logarithmically with L. With $W = 16$, keeping $\mathbb{E}[N_{\text{tail}}] < 10^{-6}$ requires $d = 16$ at $L = 64$, $d = 20$ at $L = 1024$, and $d = 31$ at $L = 10^6$.

The local-source approximation law is harsher. A finite-range surrogate for the nonlocal TT source compiler modeled by a Yukawa mass $m = 1/R$ has lowest-mode Ward residual

$$\epsilon_{\text{Ward}}(k_{\min}, R) = \frac{m^2}{k_{\min}^2 + m^2}, \qquad k_{\min} = \frac{2\pi}{L}. \tag{94}$$

Maintaining fixed Ward accuracy at the deepest box mode requires $R \propto L$. This restates the source-coupling obstruction quantitatively: exact local low-derivative TT coupling is not obtained by a finite-range compiler at fixed range.

11.2 Large-spin and finite-grid alternatives

The large-spin Holstein-Primakoff encoding

$$q_J = \frac{S_x}{\sqrt{J}}, \qquad p_J = \frac{S_y}{\sqrt{J}} \tag{95}$$

has

$$[q_J, p_J] = i\frac{S_z}{J} = i\left(1 - \frac{N}{J}\right). \tag{96}$$

At $J = 64$, with local dimension 129, the expectation-level CCR defect is 2.670584×10^{-3}. Strict operator-norm control on the tail-10^{-6} subspace is much more expensive, about 1.09375×10^{-1} at

$J = 64$. Thus the large-spin route is a valid code-sector interpretation, but direct Fock/qudit truncation is more efficient for this audited architecture.

A finite-grid/DVR oscillator can approximate individual oscillator gaps accurately at fixed target frequency, but it does not remove the basic finite-matrix trace obstruction discussed below. It is therefore a simulator regularization, not an exact local canonical algebra.

12 Why a simple protected fixed-d phase is still missing

The controlled finite-dimensional truncation does not by itself prove an exact fixed-local-dimension phase. Two obstructions remain.

12.1 Trace obstruction for exact finite-dimensional CCR

Let $A = PQP$ and $B = P\Pi P$ be finite matrices acting on a nonzero local code space. Then

$$\mathrm{tr}[A, B] = 0. \tag{97}$$

Therefore $[A, B] = iI$ cannot hold on that finite-dimensional code space. The normalized Frobenius residual lower bound is at least one for every nonzero code dimension. Exact first-class canonical brackets cannot be obtained from a finite-dimensional local code by projection alone.

This is not a problem for local low-energy simulation, where top-level population controls the defect. It is a problem for claiming an exact finite-d phase with exact onsite canonical algebra.

12.2 Onsite positive guard is relevant

A natural protection attempt is the positive onsite guard

$$V_{\mathrm{guard}} = \lambda \sum_x |d-1\rangle_x \langle d-1|_x. \tag{98}$$

The audit shows that this guard has a nonzero quadratic component in the local Gaussian vacuum and therefore opens a mass gap in the soft branch unless a counterterm is tuned. At $\lambda = 1$ the gaps are listed in Table 4.

Table 4: Onsite guard-induced gap estimates. The crossover scale is $L \sim 2\pi c/gap$.

d	Guard-induced gap	Crossover L	Expected CCR defect
5	1.044439×10^{-1}	5.99	1.938581×10^{-3}
8	7.360448×10^{-3}	85.0	9.646814×10^{-6}
10	1.190861×10^{-3}	525.6	2.569295×10^{-7}
12	1.884708×10^{-4}	3.32×10^{3}	6.569242×10^{-9}
16	4.530247×10^{-6}	1.38×10^{5}	3.976437×10^{-12}

One can fine-tune a quadratic counterterm to restore the cone, but then masslessness is tuned rather than protected by the positive guard. A successful fixed-d phase would need a many-body or symmetry protection mechanism that forbids the mass term, rather than an onsite cutoff penalty.

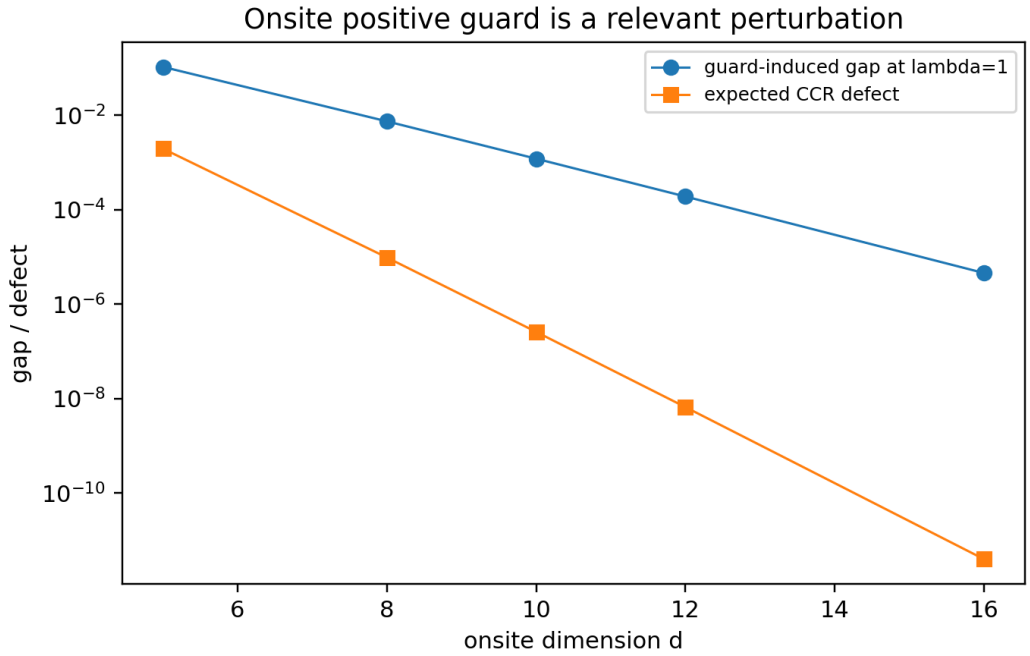

Figure 12: A positive top-level onsite guard opens a mass gap at fixed d and fixed coupling. Increasing d makes the clean finite-size window very long, but does not produce an exact fixed-d thermodynamic phase.

12.3 Global no-leakage versus local control

For local observables, fixed d controls the reduced local tail. A stronger demand, exact global no-leakage over all WL^3 oscillators, is different. The expected number of tail sites scales as

$$\mathbb{E}[N_{\text{tail}}] = WL^3\eta^d. \tag{99}$$

Therefore d must grow logarithmically with L to keep the global no-leakage probability fixed. The audit finds, for example,

L	d for $\mathbb{E}[N_{\text{tail}}] < 10^{-3}$	d for $\mathbb{E}[N_{\text{tail}}] < 10^{-6}$
64	12	16
1024	16	20
10^6	27	31

(100)

13 Interpretation

The current result occupies a precise middle ground. It is much stronger than a signed one-particle carrier and much stronger than the naive square bosonic lift. It is an exact positive local continuous-variable bosonic oscillator, and it has a finite-depth symplectic QCA implementation. It carries exactly two positive TT branches because the scalar chiral boundary mode is unique and the Stueckelberg quotient supplies exactly two polarizations. It also has a projected/conserved-source $1/k^2$ response and a CV boundary-shift symmetry protecting the origin zero mode inside the chiral family.

The topological doubling analysis clarifies why the construction had to pass through a domain wall. A single local cone in a closed periodic bulk is forbidden by charge conservation. The domain wall does not erase the mirror charge; it relocates the partner to another boundary and gaps the unwanted

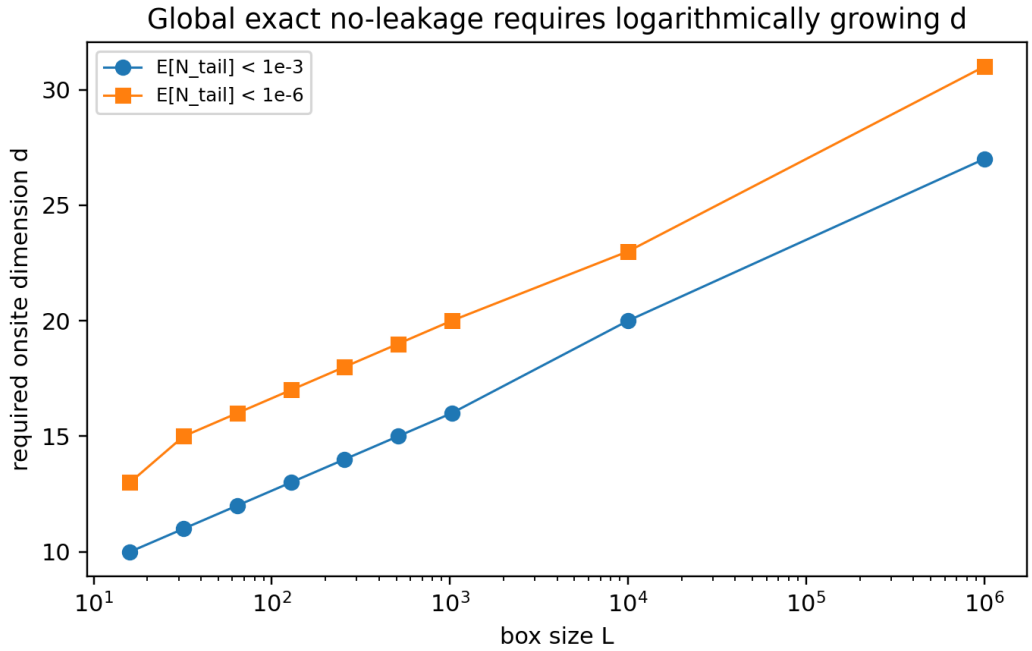

Figure 13: Fixed onsite dimension controls local reduced tails, but global exact no-leakage requires logarithmically growing d as volume increases.

boundary carrier locally. This is the same style of lesson that recurs elsewhere in the program: locality refuses a free lone cone, a low-derivative exact local TT observable, a massless mode without a protecting Ward/Goldstone mechanism, and an exact finite-dimensional canonical pair.

The honest status is therefore:

Exact CV chiral Gaussian/QCA spin-2 response carrier: achieved.
Projected/conserved-source $1/k^2$ response: achieved.
CV boundary-shift mass protection inside the chiral family: achieved.
Controlled finite-qudit truncation for local IR observables: achieved.
Exact fixed-d protected many-body phase with local universal matter coupling: not yet achieved.

(101)

Finite qudits provide controlled local simulation regularizations, but the exact canonical algebra is not finite-dimensional, the simplest positive guard is a relevant perturbation, finite-range source compilers need growing range to preserve Ward accuracy at the lowest box mode, and the Ward-completed stress sector is still an effective CV/Gaussian matter model rather than a microscopic finite-d matter Hamiltonian.

14 Next calculations

The Ward-completed audit changes the frontier. The missing object is no longer a projected response mechanism or a seagull counterterm: both have been realized in the effective CV/Gaussian theory by the local covariant square. The remaining problem is to realize the same diagonal-shift/Ward-completed square in a microscopic finite-local-dimension phase.

The most promising concrete targets are:

1. **Finite-spin or rotor Ward square.** Realize $S - \alpha h_{\mathrm{wall}}$ as a low-energy covariant difference of

finite-spin, rotor, or quantum-link variables. The audit target is not exact onsite $[Q, P] = iI$, but a thermodynamic Goldstone sector whose symmetry forbids the mass term.

2. **Microscopic matter Hamiltonian.** Build local matter degrees of freedom whose stress satisfies a dynamical Ward identity $d_i T_{ij} = 0$ and whose coupling generates the covariant square rather than an unprotected hS interaction. The test is finite TT matrix element plus no relevant self-energy.

3. **Topological-order protection.** Search for a code or ordered phase in which the diagonal shift is represented as a superselection/Goldstone symmetry and generic local wall masses are forbidden. The key diagnostic is whether generic symmetry-allowed perturbations preserve the two TT branches and $\chi_S \sim k^{-2}$.

4. **Theorem extraction.** Formalize the stability result: a finite-range positive stiffness with a simple protected wall zero, finite second gap, positive k^2 coefficient, nonzero wall/stress overlap, and a diagonal-shift Ward square has $\omega \sim |k|$ and $\chi_S \sim k^{-2}$ under all local perturbations that preserve the square structure.

5. **Finite-resource matter simulation.** Combine the truncation laws with the Ward-completed square to bound finite-d errors in the coupled stress response, including the residual gap induced by any practical local protection term.

A successful next-stage result would replace the current statement "effective CV Ward-completed spin-2 carrier with controlled finite-dimensional simulations" with "exact finite-local-dimension phase whose symmetry produces the Ward-completed square and forbids the relevant mass."

15 Conclusion

We have folded the topological doubling analysis, the chiral bosonic lift, the response/protection/approximation-law audits, and the new Ward-completed matter-coupling audit into a single spin-2 carrier manuscript. The final constructive object is a positive local continuous-variable Gaussian oscillator, with a finite-depth Gaussian QCA implementation, whose constrained TT sector has exactly two positive branches, linear dispersion, finite local boundary residue, exact first-class closure, and $1/k^2$ response to projected, auxiliary Ward-constrained, and Ward-completed stress sources.

The domain wall is understood as a topological necessity rather than an ad hoc fix: the origin cone and diagonal mirror node carry opposite winding, so the synthetic boundary construction is how the local bulk pays the Nielsen–Ninomiya doubling debt while exposing only one selected boundary cone. The chiral factorization then supplies the positive bosonic one-branch lift without squaring both signed partners.

The matter result is the new addition. A naive dynamical stress reservoir generates a relevant mass/tachyon. Completing the coupling as the local covariant square $\frac{\Omega^2}{2} \|S - \alpha h_{\text{wall}}\|^2$ ties the stress coupling and seagull by an exact diagonal shift symmetry. The coupled model retains two low positive TT branches and a Ward-stress response exponent $-1.999575\ldots$. Detuning the seagull opens a square-root mass gap or instability, and generic wall terms that violate the shift gap the pole. Thus the mass protection is real but conditional: it is enforced by the covariant-square/diagonal-shift structure, not by first-classness alone.

Controlled finite-qudit truncations remain available for local infrared observables with modest onsite dimensions, and the finite-resource laws quantify cutoff, guard, global no-leakage, and Ward-source errors. The exact protected fixed-local-dimension microscopic phase remains open. The next decisive step is a finite-spin, rotor, quantum-link, or topological-order implementation whose symmetry produces the Ward-completed square as a true local many-body mechanism.

A Numerical audit summary

Table 5: Chiral bosonic lift parameters.

Parameter	Value
r_0	0.42
r_β	2.5
c_{top}	2.0
Surface width W_{surface}	48
Scan width W_{scan}	32
First-class test width W_{FC}	8
QCA timestep τ	0.25

Table 6: Finite-dimensional truncation diagnostics.

Diagnostic	Value
Largest covariance box L	24
Covariance width W	16
Max $\langle q_s^2 \rangle$ at $L = 24$	0.397764924326
Max $\langle p_s^2 \rangle$ at $L = 24$	1.219767160624
Max $\bar{n}_s$ at $L = 24$	0.167701370515
Extrapolated max $\langle q_s^2 \rangle$	0.400151411669
Extrapolated max $\bar{n}_s$	0.170917403179
Optimized thermal ratio η	0.145968795677
d for local tail $< 10^{-6}$	8
d for local tail $< 10^{-8}$	10
d for local tail $< 10^{-10}$	12

B Ward-completed matter audit summary

C Companion internal reports

This manuscript is based on the following internal reproducibility artifacts in the same workstream:

- Normalizer/first-class audit.
- Projector/QCA audit.
- Finite-clock Floquet audit.
- Spin-2 coined/connection audit.
- Topological Cotton factorization audit.
- Stueckelberg-coined Wilson audit.
- Dynamical Stueckelberg Wilson-gap audit.

Table 7: Ward-completed dynamical matter diagnostics.

Diagnostic	Value
Matter width W	48
Coupling α	1.0
Stress oscillator scale Ω	1.0
Low positive TT branch count at $\lvert k\rvert = 10^{-3}$	2
Lowest branch exponent	0.999606677871
Second branch exponent	0.999541049078
Stress response exponent	-1.999574909721
Random Ward-stress response exponent	-1.999575423025
First gapped origin eigenvalue	0.338173473027
$\lVert D_0 v_0\rVert$	1.564×10^{-17}
Protected zero-vector residual	1.122×10^{-16}
$\lVert DT_{\mathrm{TT}}\rVert_\infty$	2.800×10^{-17}
$\lVert \mathrm{tr}\, T_{\mathrm{TT}}\rVert_\infty$	5.551×10^{-17}
Random divergence-free stress mean TT fraction	0.666936
Protected perturbation pass count	64/64
Generic unprotected gap range	$[1.773 \times 10^{-2}, 2.767 \times 10^{-1}]$

- Dynamical Wilson-partner audit.
- Topological single-cone synthetic-domain-wall audit.
- Bosonic/autonomous lift audit.
- Chiral bosonic QCA lift audit.
- Finite-local-dimension truncation audit.
- Qudit oscillator lift audit.
- Finite-qudit code/protection audit.
- Conserved-source response and Ward-stability audit.
- Local matter/Ward coupling audit.
- Dynamic matter backreaction audit.
- Gauged/Ward-completed dynamic matter audit.
- Mass-protection / boundary-shift audit.
- Finite-dimension and Ward approximation-law audit.
- Doubling-topology addendum and carrier-obstruction synthesis.

References

[1] QATNU workstream, *Normalizer first-class audit*, internal reproducibility report and bundle, June 2026.

[2] QATNU workstream, *Projector/QCA audit*, internal reproducibility report and bundle, June 2026.

[3] QATNU workstream, *Finite-clock Floquet audit*, internal reproducibility report and bundle, June 2026.

[4] QATNU workstream, *Spin-2 coined/connection audit*, internal reproducibility report and bundle, June 2026.

[5] QATNU workstream, *Topological Cotton factorization audit*, internal reproducibility report and bundle, June 2026.

[6] QATNU workstream, *Stueckelberg-coined Wilson audit*, internal reproducibility report and bundle, June 2026.

[7] QATNU workstream, *Dynamical Stueckelberg Wilson-gap audit*, internal reproducibility report and bundle, June 2026.

[8] QATNU workstream, *Dynamical Wilson-partner audit*, internal reproducibility report and bundle, June 2026.

[9] QATNU workstream, *Topological single-cone / synthetic-domain-wall audit*, internal reproducibility report and bundle, June 2026.

[10] QATNU workstream, *Bosonic/autonomous lift audit*, internal reproducibility report and bundle, June 2026.

[11] QATNU workstream, *Chiral bosonic QCA lift audit*, internal reproducibility report and bundle, June 2026.

[12] QATNU workstream, *Finite-local-dimension truncation audit*, internal reproducibility report and bundle, June 2026.

[13] QATNU workstream, *Qudit oscillator lift audit*, internal reproducibility report and bundle, June 2026.

[14] QATNU workstream, *Finite-qudit code/protection audit*, internal reproducibility report and bundle, June 2026.

[15] QATNU workstream, *Conserved-source response and Ward-stability audit*, internal reproducibility report and bundle, June 2026.

[16] QATNU workstream, *Mass-protection audit*, internal reproducibility report and bundle, June 2026.

[17] QATNU workstream, *Finite-dimension / Ward approximation-law audit*, internal reproducibility report and bundle, June 2026.

[18] QATNU workstream, *Doubling is a conservation law*, internal topology note, June 2026.

[19] H. B. Nielsen and M. Ninomiya, *Absence of neutrinos on a lattice. I. Proof by homotopy theory*, Nuclear Physics B 185, 20–40 (1981).